Int. J. Electrochem. Sci., 15 **(2020)** 2354 – 2363, doi: 10.20964/2020.03.74

International Journal of
ELECTROCHEMICAL
SCIENCE
www.electrochemsci.org

3D-flower MoS_2/Polyimide Heterostructures with Enhanced Electrochemical Properties for Lithium Storage

Peng Sun[1], *Haigang Liu*[1], *Jiahua zhao*[1], *Xiankun ma*[1], *Lehao Yang*[1], *Yongfei Wang*[1,2,*], *Zhiqiang Zhang*[1,*]

[1] School of Chemical Engineering, University of Science and Technology Liaoning, 185#, Qianshan Zhong Road, Anshan 114044, PR China
[2] School of Materials and Metallurgy, University of Science and Technology Liaoning, 185#, Qianshan Zhong Road, Anshan 114044, PR China
[*]E-mail:wyf8307@ustl.edu.cn, zzq@ustl.edu.cn

Received: 12 November 2019 / *Accepted:* 14 January 2020 / *Published:* 10 February 2020

3D-flower MoS_2/polyimide heterostructures (MoS_2/PI) with a size of 0.71 nm have been successfully synthesized through a hydrothermal and carbonization method; the above method uses water-soluble polyimide as a precursor because it contains desirable interlayer spacing and nitrogen-doped carbon. When used as anode materials in lithium-ion batteries (LIBs), the obtained nanostructures present good rate capability (226 mA h g^{-1} at 5 A g^{-1}) and superior cycling stability (490.7 mA h g^{-1} at 1 A g^{-1} over 300 cycles). We conclude that the good performance of the MoS_2/PI composite can be attributed to the high content of nitrogen doping and the abundant voids caused by the enlarged interlayer spacing of the heterostructures, both of which can buffer volume changes and create additional active sites for the LIBs. This work demonstrates that the obtained heterostructures hold great potential for high-performance energy storage applications.

Keywords: Anode materials, MoS_2, Polyimide, Nitrogen Doping, Interlayer spacing, Lithium-ion batteries

1. INTRODUCTION

Recently, LIBs have become the most dominant power source due to their high energy density, excellent security, and long cycling life.[1-4] Compared with commercial graphite anode materials, two-dimensional (2D) nanomaterials have been widely chosen as promising candidates for LIBs in view of their fascinating electrochemical performance and high safety (relatively high intercalation potential).[5,6] Among the many 2D transition metal dichalcogenides (TMDs), MoS_2 has received considerable attention for potential use in energy storage and conversion material applications;

moreover, MoS_2 has also been regarded as a promising LIB anode material because it delivers a high theoretical lithium storage capacity (670 mA h g^{-1}) compared with that of commercial graphite anodes (only 372 mA h g^{-1}).[7-9] Furthermore, MoS_2 can facilitate the intercalation of organic polymers and foreign ions as host materials.[10,11] However, MoS_2 still suffers from poor electrical conductivity and large volumetric changes during the charge-discharge process.[12]

To solve the above problems, one strategy is the integration of carbonaceous materials into MoS_2 to improve its electron transport, maintain its structural integrity during cycling, and help accommodate its volume changes. There are various decorated carbonaceous materials, for example, graphite nanocomposites, [13] reduced graphene oxide (rGO) composites, [14,15] carbon nanotube (CNT) structures,[16] and layer-by-layer MoS_2/graphene-like composites, [17,18] all of which can enhance specific capacities. The other approach is expanding the interlayer spacing since it can increase the number of reactive sites, reduce the volumetric expansion, and inhibit the accumulation of MoS_2 layers. [19-22]

Herein, we propose a simple one-step hydrothermal method to prepare 3D heterostructures composed of ultrathin-layered MoS_2 nanosheets (NSs) and polyimide as the carbonaceous material. The incorporation of polyimide as the carbon and nitrogen material into the layered MoS_2 NSs can enhance the conductivity of the whole anode and can also avoid the stacking of MoS_2 NSs; thus, well-separated ultrathin sheets are formed on the surface of PI, resulting in fully exposed active surface areas. Furthermore, the 3D framework of the MoS_2/PI composite with an expanded interlayer spacing can improve the contact area between the reaction sites and electrolyte. Therefore, the rational and novel design of 3D-heterostructured MoS_2/PI delivers excellent electrochemical properties, namely, high reversible specific capacity, cycling stability and rate capability in LIB applications.

2. EXPERIMENTAL SECTION

2.1 Material preparation

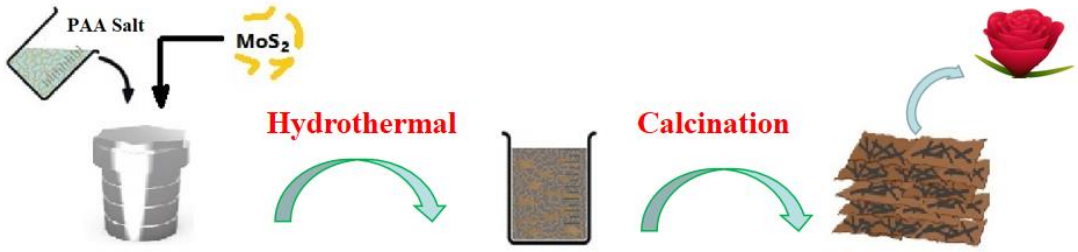

Figure 1. Schematic illustration for the synthesis of 3D flower-like MoS_2/PI.

Synthesis of the water-soluble polyimide precursor:

4,4’-ODA (0.2 g, 1 mmol) and DMF (15.86 mL) were added to a 50-mL two-necked flask equipped with a mechanical stirrer, and the solution was vigorously stirred until 4,4’-ODA was dissolved. BTDA (2 g, 1.02 mmol) was added to the stirred solution in small portions over 30 min. The reaction mixture was stirred at room temperature for 8 h and poured in 500 mL cold water to remove

DMF. The yellow precipitate was isolated by filtration, washed thoroughly with water and dried in vacuum at 50 °C for 24 h. The above PAA powder and TEA (5 mL) were added to deionized water (30 mL). Then, a yellow viscous solution of TEA-capped poly(amic acid) (TEA–PAA) was obtained.

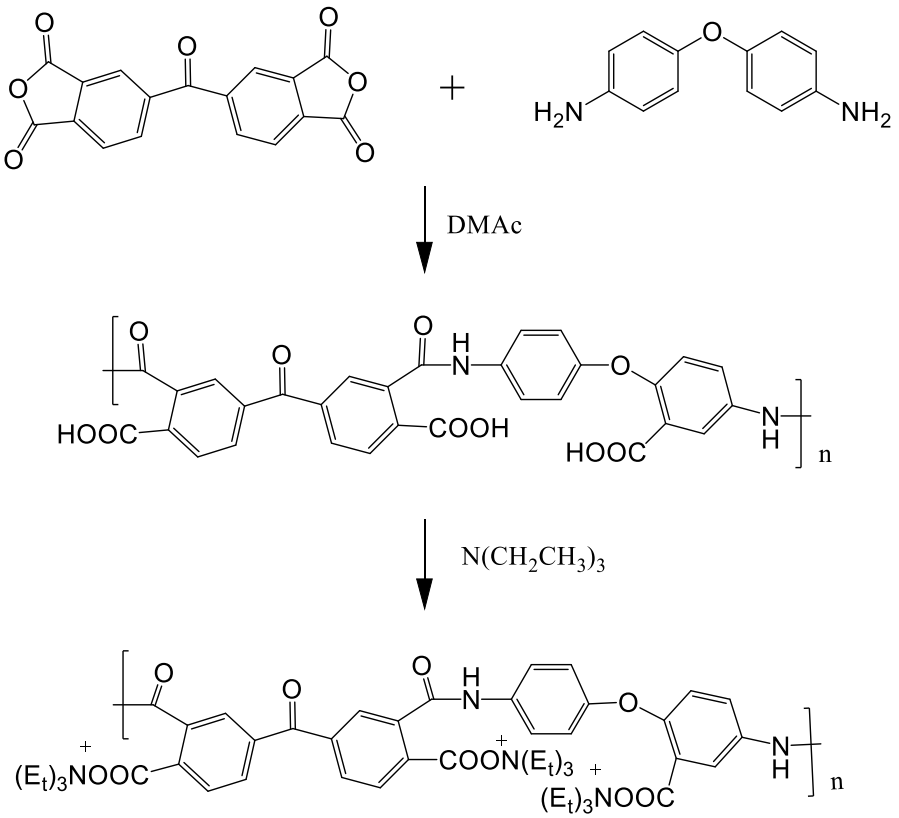

Scheme 1. Reaction route of the water-soluble polyimide precursor.

2.2. Synthesis of MoS_2/PI:

$(NH_4)_6Mo_7O_{24}•4H_2O$ (3 g) and thiourea (2.7885 g) were added to the above water-soluble polyimide solution, and the mixture was stirred. Then, the well-mixed solution was transferred to a 50-mL capacity autoclave and kept in a furnace for 18 h at 180 °C. The fabricated MoS_2/PI nanocomposite was washed, centrifuged, and dried. Finally, MoS_2/PI was obtained by annealing the product at 700 °C for 2 h at a heating rate of 3 °C min^{-1} under a N_2 atmosphere. In the case of pure MoS_2, it was prepared via an identical synthetic procedure as the MoS_2/PI nanocomposite except for the incorporation of PI.

2.3 Material Characterization

Powder X-ray diffraction (XRD, X'Pert PRO, PANalytical B.V.) patterns were collected with Cu Kα radiation (λ = 1.54178 Å). The morphologies of the as-obtained products were analyzed by scanning electron microscopy (SEM, Carl Zeiss AG, Germany). The Raman spectra were collected by a micro-Raman spectrometer (Jobin Yvon LabRam HR800) with a wavelength of 532 nm (1.96 eV) at room temperature. Transmission electron microscopy (TEM) measurements were taken with a JEM-2010F

(JEOL) transmission electron microscope operated at an accelerating voltage of 200 kV. The specific surface area was analyzed on an AutosorbIQ from Quantachrome Instruments, USA, and calculated via the Brunauer–Emmett–Teller (BET) model, while the pore size distribution was estimated by the Barret–Joyner–Halenda (BJH) method. X-ray photoelectron spectroscopy (XPS) was performed at the EPSRC NEXUS facility (Newcastle, U.K.) using monochromatic Al Kα (200 eV) as the X-ray source. DDQ (99%) was purchased from the Shenyang Sinopharm Group.

2.4. Electrochemical Characterization

For the electrochemical measurements, 2032 coin-type simulated cells were assembled. The electrolytes were $LiPF_6$ in ethyl carbonate (EC) and dimethyl carbonate (1:1) with 5 wt% fluoroethylene carbonate. A mixed slurry was prepared by dispersing MoS_2/PI (80 wt%), Super P (10 wt%), and PVDF (10 wt%) d in *N*-methylpyrrolidone (NMP), and this slurry was employed as the working electrode. Galvanostatic charge/discharge tests were conducted on a Land automatic battery tester system in a voltage window of 0–3.0 V (*vs.* Li/Li^+). Cyclic voltammetry (CV) measurements between 0.01 and 3.0 V at a scan rate of 0.2 mV s^{-1}, and EIS with a frequency range of 10^{-2}-10^5 Hz was performed on a Vertex.C. DC power supply (Metrohm, Netherlands).

3. RESULTS AND DISCUSSION

The synthesis of MoS_2/PI 3D-flower heterostructures is illustrated in Figure 1. First, a water-soluble polyimide precursor of PAA salt was prepared. Afterward, the MoS_2/PI nanocomposite was fabricated in situ using a facile hydrothermal method. Finally, the PI/MoS_2 nanocomposites were calcined in a N2 atmosphere.

We first examined the morphologies of the MoS_2/PI and pristine MoS2 products using SEM measurements. An SEM image of MoS_2/PI in Figure 2a shows that these well-dispersed particles presented uniform 3D-flower heterostructures with a diameter of approximately 300 nm. As depicted in Figure 2a and 2b, ultrathin MoS_2 flowers were anchored onto the PI carbon surface. Furthermore, transmission electron microscopy (TEM) was used to characterize the morphologies. It can be clearly observed that the MoS_2 heterostructures displayed an expanded interlayer distance of approximately 0.71 nm, which is wider than that of bare MoS_2 (0.62 nm) (Figure 2c). The results illustrated that the large d-spacing on the c axis can be ascribed to the intercalation of amorphous carbon species into the interlamellar spacing during polyimide pyrolysis.[23,24] In addition, Figure 2d shows that the MoS_2/PI composites show 3D-interconnected porous heterostructures, which can further indicate that the MoS_2 NSs are decorated on the PI surface. Figure 2f shows that the selected diffraction patterns can be assigned to the (100), (103), and (110) planes of MoS_2. Furthermore, an energy-dispersive X-ray (EDX) mapping analysis of a single nanosphere shows that all the chemical elements are uniformly distributed on the whole 3D-PI carbon surface.

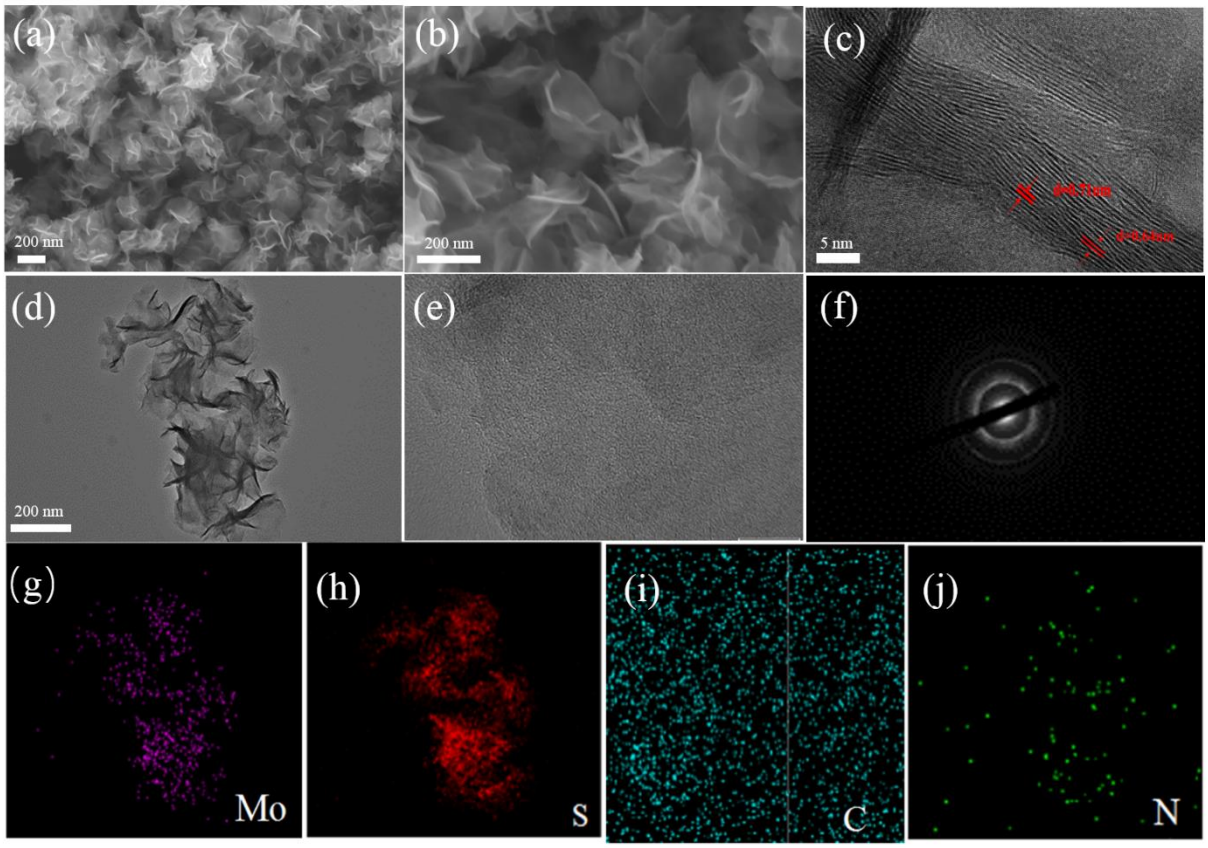

Figure 2. (a) SEM image of the MoS_2/PI hybrids, (b) low-, and (c) high-magnification TEM images, (d) high-resolution TEM images, (f) the corresponding SAED pattern, and the (g–j) TEM-EDS mapping of the as-synthesized MoS_2/PI hybrids.

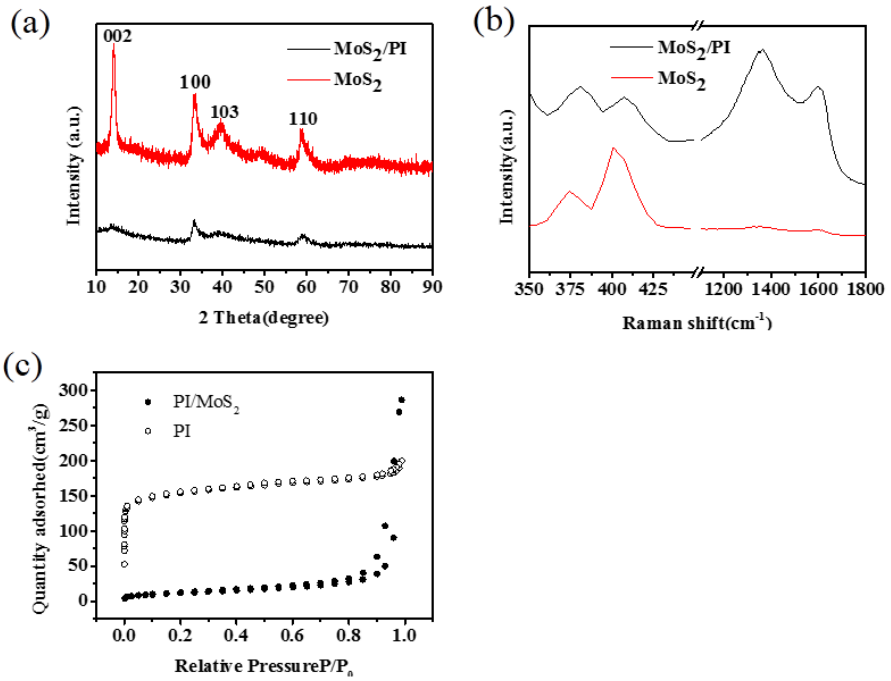

Figure 3. (a) XRD patterns of the MoS_2/PI hybrids, (b) Raman spectra of MoS_2@PI and the annealed MoS_2, and (c) N_2 adsorption/desorption isotherms of MoS_2@PI and the annealed PI.

The XRD patterns of the as-prepared MoS_2/PI nanostructures are shown in Figure 3a, and all diffraction peaks correspond to hexagonal MoS_2. The MoS_2/PI shows a weak (002) face, indicating few-layered MoS_2 nanosheets are loaded on polyimide compared to that of pristine MoS_2, which is in good agreement with the HRTEM results. As clearly seen in Figure 3b, both Raman spectra presents two peaks at approximately 370 and 408 cm^{-1} that are attributed to the in-plane (E^12g) and out-of-plane vibrations (A1g) of MoS_2;[25,26] the above peaks correspond to the typical first-order Raman active modes E2g and A1g due to in-plane vibrational modes within the S–Mo–S layer. In addition, two other peaks at 1394.5 and 1599.5 cm^{-1} appear in the spectrum of MoS_2/PI, which are indexed to the D and G bands of carbon, thus confirming the existence of a carbon coating in the composites. Furthermore, the specific surface area of the 3D-PI carbon skeleton was characterized (Figure 3c). Compared with the PI carbon skeleton (the specific surface area is 590 $m^2\ g^{-1}$) with many mesopores, the MoS_2/PI delivers a small specific surface area (42 $m^2\ g^{-1}$) due to the in situ growth of MoS_2 NSs on the 3D-PI carbon surface. It is believed that a mesoporous structure can facilitate the transport of lithium ions and reduce the volume expansion during the cycling process.

X-ray photoelectron spectroscopy (XPS) measurements were conducted to explore the surface components and chemical states of the MoS_2/PI nanostructures. The spectrum shows that Mo, S, C, and N exist in the composite with a 1/2 Mo/S atomic ratio. Figure 4b clearly shows two peaks located at 228.2 and 232.4 eV, which are assigned to $Mo_{5/2}$ and $Mo_{3/2}$ in the Mo(IV) state. In addition, the peak at 226.8 eV can be indexed to S 2s. As shown by the high-resolution spectrum (Figure 4d), S 2p can be deconvoluted into S $3p_{3/2}$ and S $3p_{1/2}$ (161.9 and 162.8 eV, respectively), which proves the existence of stoichiometric MoS_2. Figure 4c shows that the N 1s core level can be deconvoluted into two peaks at 397.8 and 398.4 eV; these peaks correspond to pyridinic- and pyrrolic-N derived from the PI carbon skeleton, respectively. Furthermore, the content of nitrogen in the MoS_2/PI nanostructures is 1.48 wt.% according to the high-resolution spectrum. [27] Nitrogen doping can introduce vacancies and electron deficiencies, which is beneficial for the kinetic process of lithium storage. It can also facilitate lithium penetration into host materials, leading to enhanced electrochemical performance.

The electrochemical lithium storage activity of MoS_2/PI nanostructures was investigated by CV measurements. Figure 5a presents the initial 3 cycle voltage profiles at a scanning rate of 0.01 mV s^{-1} over a potential range of 3.0 to 0.01 V. There are two peaks at approximately 1.1 V and 0.4 V in the first cycle, which is consistent with previous reports. [28-29] The peaks at 1.1 V can be considered lithium insertion into an interlayer of MoS_2 to form Li_xMoS_2, accompanied by a phase transformation from the 2H to 1T structure of Li_xMoS_2. The second main peak located at 0.4 V is associated with the further reaction between Li_xMoS_2 and Li ions, resulting in Li_2S and metallic Mo particles. We can also observe that the two cathodic peaks disappear in the next cycles, and the results indicate irreversibility in the conversion of MoS_2 into Li_2S and Mo. Two peaks located at approximately 1.62 and 2.32 V can be clearly seen in the charging process. The weak peak at 1.62 V is assigned to Li^+, which is indicative of Mo reduction. In addition, the pronounced peak at 2.32 V is associated with the conversion of Li_2S to sulfur or polysulfide. [30-33] Notably, they are almost unchanged and remain stable after the first cycle in the CV curves, which demonstrates good stability and high reversibility in the LIBs. Figure 6b and 6c show the charge-discharge profiles of bulk MoS_2 and MoS_2/PI at a current density of 0.1 A g^{-1}. The results are consistent with the CV curves at approximately 1.1 V and 0.6 V when compared with the

total reaction process: $MoS_2 + 4\ Li \rightarrow Mo + 2\ Li_2S$.[34,35] The initial discharge capacity of MoS_2/PI is 1039.2 mA h g^{-1}, and the corresponding charge capacity is 831.1 mA h g^{-1}; additionally, it has a coulombic efficiency of approximately 80%. The relatively low coulombic efficiency in the initial cycle can be attributed to some irreversible processes, such as the formation of the solid electrolyte interface or ined at nearly 98% in the second cycle. As shown in Figure 6c and 6d, the rate capability was analyzed at various current densities from 0.1 A g^{-1} to 5 A g^{-1}. Obviously, discharge capacities of approximately 744.3, 620.8, 595.7, 504.4, 374.9, and 226 mA h g^{-1} are achieved for MoS_2/PI at 0.1, 0.2, 0.5, 1, 2 and 5 A g^{-1}, respectively, while bulk MoS_2 delivers lower capacities of 662.5, 439.5, 146.7, 23.2, 3.9 and 2.1 mA h g^{-1}, respectively. In addition, the cycling stability of MoS_2/PI was evaluated at a large current density of 1 A g^{-1}, the specific discharge capacity is able to retain a reversible capacity of ~490 mA h g^{-1} with a coulombic efficiency of approximately 80%, and the capacity has nearly no fading after almost 300 cycles. Moreover, the specific capacitance of MoS_2/PI is close or higher than that of some of the previously reported graphite-like carbon based MoS_2 anode materials (see Table 1) when measured at the same current density.

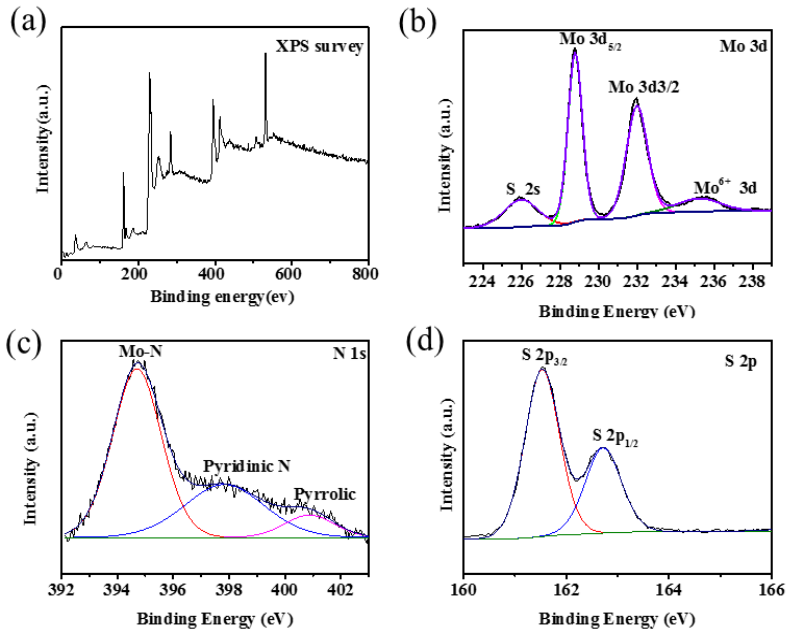

Figure 4. XPS spectra of MoS_2/PI: a) survey spectrum and high-resolution spectra of Mo 3d (b), N 1s (c), and S 2p (d).

Table 1. Comparison of specific capacitances between the current work and relevant reports.

Ref.	Samples	discharge capacity (mAh g^{-1})
13	MoS_2-graphite	720 (0.1 A g^{-1}) 472 （1 A g^{-1}）
14	MoS_2-RGO	724 (0.05 A g^{-1}) 320 （2.5 A g^{-1}）

15	Layered MoS_2/Graphene	1100 (0.1 A g^{-1}) 900 (1 A g^{-1})
16	3D graphene@CNT@MoS_2 hybrid foam	935 (0.1 A g^{-1}) 528 (1 A g^{-1})
17	2D MoS_2/mesoporous dopamine carbon	744 (0.1 A g^{-1}) 480 (1.6 A g^{-1})
19	Layered MoS_2	842 (0.1 A g^{-1}) 546 (1 A g^{-1})
20	TiO_2 nanowire@MoS_2 nanosheet	581 (0.1 A g^{-1}) 470 (0.5 A g^{-1})
21	MoS_2-rGO hollow carbon spheres	1145 (0.1 A g^{-1}) 753 (2 A g^{-1})
23	glucose-assisted carbon-coated MoS_2	785.9 (0.1 A g^{-1}) 585.6 (1 A g^{-1})
Current work	MoS_2/polyimide	744.3 (0.1 A g^{-1}) 490.7 (1 A g^{-1})

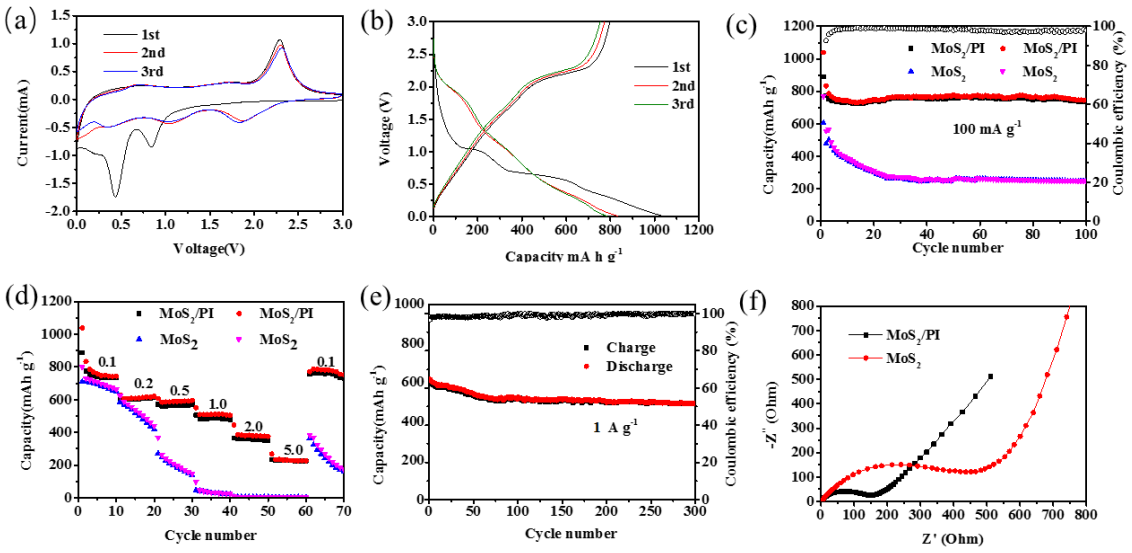

Figure 5. (a) CV curves at 0.01-3 mVs^{-1} with a scan rate of 0.2 mV s^{-1} and (b) cycling performances of the MoS_2/PI hybrids, the MoS_2@PI hybrids and the annealed MoS_2. (c) Galvanostatic charge-discharge profiles at current densities of 0.1 A g^{-1} and at various current densities with the MoS_2/PI hybrids. (d) Rate capabilities and cycling performances (0.1 A g^{-1}) of the bare MoS_2 and MoS_2/PI hybrid electrodes. (e) Long cycling performance (1 A g^{-1}) of the MoS_2/PI composite electrode. (f) Nyquist plots of the bulk MoS_2 and MoS_2/PI hybrids.

To further understand the electrical conductivity of the MoS_2/PI nanostructure, electrochemical impedance spectroscopy (EIS) was also carried out and is illustrated in Figure 5f. The semicircle in the high-frequency region represents the interfacial impedance (resistance of the SEI film and the charge-transfer resistance (R_{ct})), while the sloped line in the low-frequency region represents the solid-state

diffusion resistance of Li^+ in the bulk of the electrode. [36] The relatively low *Rct* values of the MoS_2/PI electrode compared with that of the pristine MoS_2 can be attributed to both the nitrogen-doped carbon and expanded interlayer spacing in MoS_2. These features provide the low charge transfer resistance and high Li-ion diffusion rate of the MoS_2/PI electrode, thus demonstrating excellent electrochemical performance.

4. CONCLUSION

In summary, a 3D-flower MoS_2/PI heterostructure was prepared though a facile hydrothermal and carbonization method using water-soluble PI as a precursor. The materials exhibit good electrochemical LIB performances, demonstrating high specific capacity, cycling stability, and good rate performance after the charge-discharge process. The good performance of the MoS_2/PI composite can be attributed to the synergistic effects between MoS_2, with expanded interlayer spacing, and the 3D-PI carbon. The MoS_2/PI composite holds great potential for high-performance energy storage applications.

ACKNOWLEDGMENTS
We gratefully acknowledge the Natural Science Foundation of Liaoning Province (No. 2019-ZD-0266).

References

1. M.R. Palacin, M. Rosa, *Chem.Soc. Rev.,* 38 (2009) 2565.
2. M. Armand, J. M. Tarascon, *Nature,* 451 (2008) 652.
3. Y. Lu, Z.Tu, and L. A. Archer, *Nat. Mater.,* 13 (2014) 961.
4. L. Lin, Z. Ji, M. Alcoutlabi and X. Zhang, *Energy Environ. Sci.,* 4 (2011) 2682.
5. S. Xiao, X. Li, W. Sun, B. Guan and Y. Wang, *Biochem. Eng. J.,* 306 (2016)251.
6. K. Chang, W. Chen, *ACS nano,* 5 (2011) 4720.
7. J. Zhou, J.Qin, X. Zhang, C. Shi, E. Liu, J. Li, N. Zhao, and C. He, *ACS Nano,* 9(2015)3837.
8. X. Yu, H. Hu, Y. Wang, H. Chen and X. Lou, *Angew. Chem.Int. Ed.,*127 (2015) 7503.
9. X. Yu, L. Yu and X. Lou, *Small Methods,* 1 (2017) 1600020.
10. Y. Sun, F. Alimohammadi, D. Zhang and G. Guo, *Nano Lett.*, 17(2017)196.
11. K.F. Mak, C. Lee, J. Hone, J. Shan, and T.F. Heinz, *Phys. Rev. Lett,* 105 (2010) 136805.
12. Q. Zhu , C. Zhao, Y. Bian , C. Mao, H. Peng, and G. Li, *Synth. Met.,* 235(2018)103.
13. H. Zhao, H. Zeng, Y. Wu, S. Zhang, B. Li, and Y. Huang, *J. Mater. Chem. A,* 3 (2015)10466.
14. M. Choi, S. K. Koppala, D. Yoon, J. Hwang, S. M. Kim and J. Kim, J. Power Sources, (309)2016,202.
15. K. Chang and W.X. Chen, *ACS nano,* 5 (2011) 4720-4728.
16. J. Ren, R.P. Ren and Y.K. Lv, *Chem. Eng. J., 3*53(2018). 419
17. H. Jiang, D. Ren, H. Wang, Y. Hu, S. Guo, H.Yuan, P. Hu, L. Zhang and C. Li, *Adv. Mater.,* 27(2015)3687.
18. C. Chen, Z. Feng, Y. Feng, Y. Yue, C. Qin, D. Zhang and W. Feng, *ACS Appl. Mater. Interfaces,* 8(2016)19004.
19. G. Du, Z. Guo, S. Wang, R. Zeng, Z. Chen and H. Liu, *Chem. Commun.,* 46 (2010) 1106.
20. D. Zhang, A. Pan, X. Zhong, H. Song Y. J. Yong and J. Wang, *Alloys Compd.,* 758(2018)91.
21. X. Hu, Y. Li, G. Zeng, J. Jia, H. Zhan, Z. Wen. Three-Dimensional Network Architecture with Hybrid Nanocarbon Composites Supporting Few-Layer MoS_2 for Lithium and Sodium Storage. ACS Nano, 12 (2018) 1592.

22. L. Jing, G. Lian, F. Niu, J. Yang, Q. Wang, D. Cui, C. P. Wong, and X. Liu. Nano Energy, 51(2018)546.
23. B. Chen, E. Liu, F. He, C. Shi, C. He, J. Li and N. Zhao, Nano Energy, 26(2016)541.
24. B. Chen, N. Zhao, L. Guo, F. He, C. Shi, C. He, J. Li and F. Liu, Nanoscale, 7(2015)12895.
25. Y. Jiao, A. Mukhopadhyay, Y. Ma, L. Yang, A. M. Hafez and H. Zhu, Adv. Energy Mater., 8(2018)1702779.
26. J. Yang, K. Wang, J. Zhu, C. Zhang and T. Liu, *ACS Appl. Mater. Interfaces, 8(*2016)31702.
27. J. Jiang, P. Nie, B. Ding, Y. Zhang, G. Xu, L. Wu, H. Dou and X. Zhang, *J. Mater. Chem. A.,* 5(2017)23283.
28. L. Zhang and X.W. Lou, *Chemistry - A European Journal,* 18(2014) 5219.
29. X. Zhou, L. Wang and G. Guo, *Nanoscale,* 4 (2012) 5868.
30. X. Zhang, and B. Tan, *Int. J. Electrochem. Sci.,* 13 (2018) 11388.
31. Q. Pang, Y. Zhao, X. Bian, Y. Ju, X. Wang, Y. Wei, B. Liu, F. Du, C. Wang and G Chen, *J. Mater. Chem. A.,* 5 (2017)3667.
32. Z. Wang, T. Chen, W. Chen, K. Chang, L. Ma, G. Huang, D. Chen and J.Y. Lee, *J. Mater. Chem. A*, 1(2013), 2202.
33. Y. Cai, H. Wang, S. Zhuan, J. Jin, C. Wang, Y. Yu, Y. Li, B. Su, *Sci. Rep.,* 5 (2015) 11557.
34. N. Li, Z. Liu, Q. Gao, X. Li, R. Wang, X. Yan and Y. Li, *J. Mater. Sci.,* 52(2017), 13183.
35. B. Li, R. Qi, J. Zai, F. Du, C. Xue, Y. Jin, C. Jin, Z. Ma, X. Qian, *Small,* 12(2016) 5281.
36. Y. Zhou, Y. Liu, W. Zhao, F. Xie, R. Xu, B. Li, X. Zhou and H. Shen, *J. Mater. Chem. A.,* 4 (2016) 5932.